

## Measurement of magnetic fluctuation-induced particle flux (invited)<sup>a)</sup>

W. X. Ding, D. L. Brower, and T. Y. Yates

Department of Physics and Astronomy, University of California-Los Angeles, Los Angeles, California 90095, USA

(Presented 13 May 2008; received 12 May 2008; accepted 16 May 2008; published online 31 October 2008)

Magnetic field fluctuation-induced particle transport has been directly measured in the high-temperature core of the MST reversed field pinch plasma. Measurement of radial particle transport is achieved by combining various interferometry techniques, including Faraday rotation, conventional interferometry, and differential interferometry. It is observed that electron convective particle flux and its divergence exhibit a significant increase during a sawtooth crash. In this paper, we describe the basic techniques employed to determine the particle flux. © 2008 American Institute of Physics. [DOI: 10.1063/1.2953437]

### I. INTRODUCTION

Particle transport arising from stochastic magnetic fields has long been an important and unresolved topic in fusion research.<sup>1-4</sup> Stochastic magnetic fields can arise from global tearing instabilities that often underlie the sawtooth oscillation, and cause anomalous particle, momentum, and energy transport. Conversely, externally imposed magnetic perturbations can act to mitigate edge-localized modes by locally enhancing edge transport without loss of core plasma confinement and have generated new interest in understanding the role played by stochastic magnetic fields in transport.<sup>5,6</sup>

Stochastic magnetic field induced particle transport can be described as the projection of the parallel particle flux along the radial direction in a toroidal device,<sup>7</sup>

$$\Gamma_{r,\alpha} = \langle \Gamma_{\parallel,\alpha} \vec{b} \cdot \vec{e}_r \rangle, \quad (1)$$

where  $\Gamma_{\parallel,\alpha} = n_\alpha V_{\parallel,\alpha}$  is parallel particle flux for species  $\alpha$  (electron or ion),  $\vec{b} = \vec{B}/B$  is a unit vector of magnetic field,  $\vec{e}_r$  is a radial unit vector,  $\langle \dots \rangle$  denotes a magnetic surface average, and  $V_{\parallel,\alpha}$  is particle parallel velocity. Both the parallel flux and magnetic field can be decomposed into mean and fluctuating components, i.e.,  $\Gamma_{\parallel,\alpha} = \Gamma_{\parallel 0,\alpha} + \delta\Gamma_{\parallel,\alpha}$ ,  $\vec{b} = \vec{b}_0 + \delta\vec{b}$ . Thus, the magnetic fluctuation-induced radial particle flux can be written as

$$\Gamma_{r,\alpha} = \frac{\langle \delta\Gamma_{\parallel,\alpha} \delta b_r \rangle}{B}, \quad (2)$$

where  $\delta\Gamma_{\parallel,\alpha}$  is the fluctuating flux parallel to the magnetic field  $\vec{B}$ , and  $\delta b_r$  is the radial magnetic field fluctuation. The mean radial magnetic field component is zero. Fluctuating parallel flux arises from density and parallel velocity fluctuations according to the relation  $\delta\Gamma_{\parallel,\alpha} = V_{\parallel,\alpha} \delta n + n \delta V_{\parallel,\alpha}$ . Therefore, we can rewrite Eq. (2) as

$$\Gamma_{r,\alpha} = \frac{\langle \delta\Gamma_{\parallel,\alpha} \delta b_r \rangle}{B} = V_{\parallel,\alpha} \frac{\langle \delta n \delta b_r \rangle}{B} + n \frac{\langle \delta V_{\parallel,\alpha} \delta b_r \rangle}{B}, \quad (3)$$

where  $n(\delta n)$ ,  $B(\delta b_r)$ , and  $V_{\parallel}(\delta V_{\parallel})$  are density, magnetic field, and parallel velocity equilibrium (fluctuating) quantities. The first term on the right hand side of Eq. (3) is the convective particle flux and the second term is referred to as a “pinch” term, which can be directed either inward or outward. Furthermore, the derivative of particle flux must be measured in order to infer a local density change. This can be easily seen from particle conservation equation, neglecting particle source,

$$\frac{\partial n}{\partial t} + \nabla \cdot \Gamma_r = 0, \quad (4)$$

where the divergence of radial flux balances the density change.

Experimental determination of the various fluctuating quantities and their correlations, according to Eq. (3), in the core of a high-temperature plasma is extremely challenging. Both fast time response and good spatial resolution are required. Herein, we discuss the measurement of (1) density fluctuations and their spatial derivative by conventional and differential interferometry, and (2) magnetic fluctuations by Faraday rotation. By evaluating the correlated product of these quantities, the magnetic fluctuation-induced particle flux and its divergence are determined.

### II. DIFFERENTIAL INTERFEROMETRY TECHNIQUE

#### A. Principle of differential interferometry

In principle, the measurement of local electron density  $n(r)$  requires a differential measurement. As is well known, the phase change in a laser beam induced by plasma in a cylindrical geometry is given by

$$\varphi(x) = r_e \lambda \int_{-\sqrt{a^2-x^2}}^{\sqrt{a^2-x^2}} n(r) dz, \quad (5)$$

where  $r_e = 2.82 \times 10^{-15}$  m is the classical electron radius,  $\lambda$  is the laser wavelength,  $z$  is the distance along the chord,  $x$  is

<sup>a)</sup>Invited paper, published as part of the Proceedings of the 17th Topical Conference on High-Temperature Plasma Diagnostics, Albuquerque, New Mexico, May 2008.

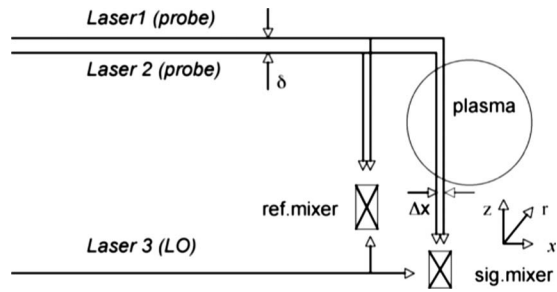


FIG. 1. Schematic of the differential interferometer experimental setup. Note that beam offset at the source ( $\delta$ ) and in the plasma ( $\Delta x$ ) are different due to an optical system with out-of-plane non-45° bends that are not pictured.

the impact parameter, and  $x^2 + z^2 = r^2$ . The local density is found by performing a standard Abel inversion<sup>8</sup> using

$$n(r) = -\frac{1}{\pi r_e \lambda} \int_r^a \frac{\partial \varphi(x)}{\partial x} \frac{dx}{\sqrt{x^2 - r^2}}. \quad (6)$$

From this relation it is clear that the first spatial derivative of the phase,  $\partial \varphi / \partial x$ , is required to obtain  $n(r)$ . Conventional interferometers measure  $\varphi(x)$  for multiple discrete chords, make a numerical fit to the available points, take the spatial derivative to infer  $\partial \varphi / \partial x$ , and then perform an inversion. The number of chords determines the accuracy of density measurement. The difficulty in directly measuring  $\partial \varphi / \partial x$  is that the phase difference becomes smaller as two adjacent chords are brought closer together, and physical separation between adjacent detectors usually limits the spatial resolution. These difficulties can be overcome by employing a new differential heterodyne interferometer technique.

The differential heterodyne interferometer system employed on MST utilizes two parallel linearly polarized, spatially offset far infrared (FIR) laser beams ( $\lambda = 432 \mu\text{m}$ ) with frequency difference  $\sim 1$  MHz to probe the plasma at each chord position ( $x$ ) as shown in Fig. 1. Other relevant details of the system hardware have been described elsewhere.<sup>9</sup> The two parallel laser beams are initially slightly offset a small distance ( $\delta$ ) and then divided into 11 separate chords by wire mesh beamsplitters. The phase difference between these two probing beams at each chord position with respect to a reference signal is obtained directly using a digital phase comparator technique in order to determine  $\Delta \varphi(x, t)$ . Furthermore, a single detector is used to measure the phase between the two spatially separated beams so that beam offset can be reduced to zero. In this new configuration, referred to as a differential interferometry, the system is insensitive to path length changes due to vibrations and thermal expansion effects since both probing beams traverse nearly identical optical paths, have wavelength difference of only  $\Delta \lambda / \lambda = 10^{-6}$ , and use the same optical elements including mixer. In addition, the measured phase difference can be controlled, by varying the spatial offset, and set to  $< 2\pi$  thereby eliminating the potential for fringe counting errors.

In this configuration, the system has a fast time response, up to  $1 \mu\text{s}$ , and phase noise less than  $0.05^\circ$  for 20 kHz bandwidth. A third FIR laser (also frequency offset), serves as a local oscillator beam for each mixer to permit simultaneous

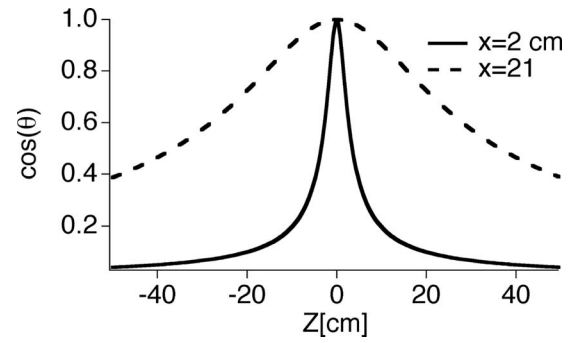


FIG. 2. The cosine weighted factor changes along beam path for two different impact parameters.

measurement of  $\varphi(x, t)$  via the conventional interferometry approach. The effective displacement between two beams is  $\delta \sim 1$  mm, which is obtained from calibration.<sup>10</sup> The calibration procedure is performed by comparing density profile measured by differential interferometer to profile by conventional interferometer. Once the differential interferometer is calibrated, it can be operated independently to measure density, density fluctuations, and their gradients.

## B. Localization of density fluctuation measurements

The differential interferometer determines the phase difference between two adjacent beams and provides a line-integrated density gradient measurement,  $(\partial / \partial x) \varphi(x)$ . However, this line-integrated measurement is weighted by a geometrical factor. Upon taking the first spatial derivative of Eq. (5), we find

$$\begin{aligned} \frac{\partial \varphi(x)}{\partial x} &= r_e \lambda \int \frac{\partial n(r)}{\partial r} \frac{\partial r}{\partial x} dz = r_e \lambda \int \frac{\partial n(r)}{\partial r} \frac{x}{r} dz \\ &= r_e \lambda \int \frac{\partial n(r)}{\partial r} \cos(\theta) dz, \end{aligned} \quad (7)$$

where  $\cos \theta = x/r$ . The cosine term is a geometrical weighting factor and is shown in Fig. 2, for different impact parameters. As the impact parameter approaches zero, the weighting factor is reduced in width and approaches a delta function, thereby providing spatial resolution. For small impact parameter  $x$ , differential interferometry essentially provides a localized measurement of the density gradient and density gradient fluctuations. This cosine weighting factor has previously been used to analyze Faraday rotation data to obtain central safety factor  $q_0$ .<sup>11</sup>

Mathematically, Eq. (7) can be simplified as  $x \rightarrow 0$ ,  $r \rightarrow 0$ ; the density gradient can be expanded in a Taylor series,  $\partial n(r) / \partial r \approx (\partial / \partial r) n(0) + r (\partial^2 / \partial r^2) n(0)$ , allowing one to rewrite Eq. (7) as  $\partial / \partial x \varphi(x \rightarrow 0) = r_e \lambda x (\partial^2 / \partial r^2) n(0) L$  (where  $L$  is the path length), leading to

$$\frac{\partial}{\partial r} n(r) \approx \frac{\partial}{\partial x} \varphi(x) \frac{1}{r_e \lambda L} \Big|_{x=r \rightarrow 0}. \quad (8)$$

From Eq. (8), it is found that the differential phase is proportional to the density gradient for measurements made near the magnetic axis. This approximation offers the great convenience of being able to directly determine the local particle

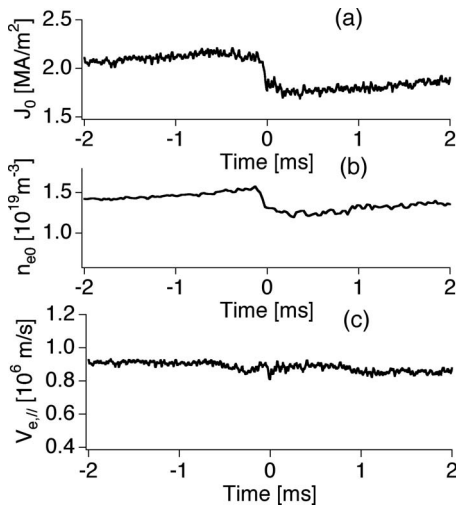


FIG. 3. (a) Time history of current density; (b) time history of equilibrium density; (c) time history of electron parallel velocity at magnetic axis.  $t=0$  denotes sawtooth crash.

flux without performing any Abel inversion of the line-integrated density measurements.

In general, density fluctuations can be written as  $\tilde{n} = \sum \tilde{n}_{m,n}(r) \cos(m\theta + n\phi)$  where  $m, n$  are poloidal and toroidal mode number, respectively. In MST, the dominant modes have  $m=1$  and the fluctuating phase measured by conventional interferometry is given by

$$\delta\varphi(x) = r_e \lambda \int \delta n_{m=1}(r) \cos(\theta) dz, \quad (9)$$

where  $\cos(\theta)$  is the same geometrical weighting factor that appears in Eq. (7). The fluctuating density can then be written approximately as  $\delta n(r) = \delta n(0) + r(\partial/\partial r)\delta n(0)$ ,  $x \rightarrow 0$ ,  $r \rightarrow 0$ . This leads to a simple relation between phase fluctuation and density fluctuation for chords close to plasma center,

$$\delta n(r) \approx \delta\varphi(x) \frac{1}{r_e \lambda L} \Big|_{x=r \rightarrow 0}. \quad (10)$$

It should be noted that Eq. (10) is applicable to mode number  $m=1$  only since the cosine factor arises from the nature of mode. However, Eq. (8) is generally applicable to all modes since the weighting factor in Eq. (7) results from differential interferometer technique itself and is independent of mode structure. Both relations Eqs. (8) and (10) are applicable to chords close to magnetic axis.

For viewing lines of sight away from plasma center, one has to deal with an asymmetric fluctuation inversion.<sup>12</sup> Herein, we will focus on the measurements close to plasma center so that the convective particle flux can be directly measured without requiring more sophisticated fluctuation inversion methods.

### III. DENSITY FLUCTUATION MEASUREMENT

Experiments have been performed on the MST RFP, a circular cross-section device with major radius  $R=1.5$  m, minor radius  $a=0.52$  m, discharge current  $I_p \leq 600$  kA, line-average electron density  $n_e \sim 1 \times 10^{19} \text{ m}^{-3}$ , and electron tem-

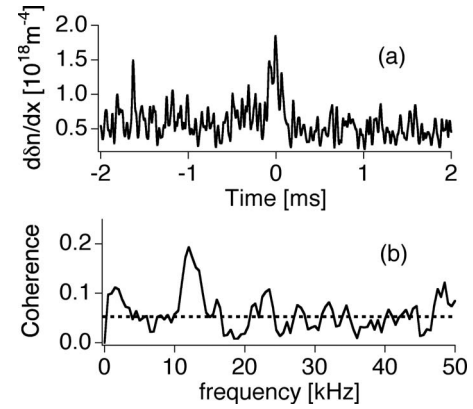


FIG. 4. (a) Time history of density gradient fluctuations; (b) the coherence between density gradient fluctuation and magnetic fluctuation. The significant coherence appears for tearing mode frequency between 10 and 20 kHz. The measurement is made at  $r/a=0.11$  near magnetic axis.

perature  $T_e \leq 1$  keV. Many parameters in MST plasmas display a sawtooth cycle due to relaxation oscillations in the plasma core. To determine the time evolution of mean (magnetic surface averaged) quantities, we ensemble average measured quantities over many reproducible sawtooth events, thereby eliminating the contribution of random fluctuations. A typical MST discharge history over a sawtooth cycle is shown in Fig. 3. The current density has a slow, linear ramp phase before a sawtooth crash and promptly drops within 200  $\mu\text{s}$  at the crash, as shown in Fig. 3(a). The equilibrium electron density at the magnetic axis relaxes as well [see Fig. 3(b)], and the relaxation time is much faster than the classical diffusion time [ $\sim 1$  s]. The inferred electron mean velocity shows a little change over sawtooth crash [see Fig. 3(c)]. The fast density collapse implies significant fluctuation-induced particle transport during the sawtooth crash.

Density fluctuations and density gradient fluctuations [see Eqs. (8) and (10)] can be directly measured by both conventional interferometry and differential interferometry. Density gradient fluctuations exhibit significant increase at sawtooth crash as shown in Fig. 4(a), and have a coherence with the radial magnetic fluctuation [ $m=1$ ,  $n=6$  mode] as shown in Fig. 4(b). Coherence peaks in the 10–20 kHz range, corresponding to tearing mode activity for the dominant core-resonant mode. The dashed line denotes the statistical noise level determined by the number of ensembles. Density fluctuations have a similar temporal dynamics to density gradient fluctuations and have been investigated previously.<sup>12</sup>

### IV. MAGNETIC FLUCTUATION MEASUREMENT BY FARADAY ROTATION

Equilibrium and fluctuating magnetic fields in MST are measured by polarimetry making use of the Faraday effect. The Faraday rotation angle  $\Psi$  is half the phase difference between the  $R$ - and  $L$ -wave refractive indices and can be written as

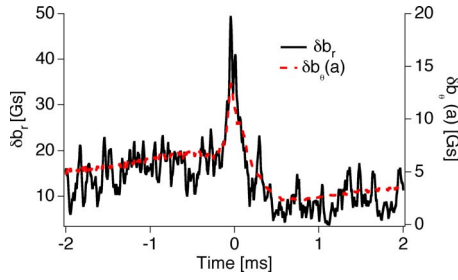


FIG. 5. (Color online) The line-integrated radial magnetic field fluctuation (left vertical axis) varies over sawtooth cycle. The dashed line shows poloidal magnetic field fluctuation (right vertical axis) measured at wall. The zero denotes sawtooth crash.

$$\Psi = \frac{2\pi}{\lambda} \int \frac{(N_R - N_L)}{2} dz = 2.62 \times 10^{-13} \lambda^2 \int n_e B_z dz, \quad (11)$$

where  $B_z$  is magnetic field component along the laser beam,  $n_e$  is the electron density,  $\lambda$  is the FIR laser wavelength, and  $z$  is the plasma cross-section vertical coordinate, all in MKS units. Taking  $\Psi = \Psi_0 + \tilde{\Psi}$  and  $B_z = B_{z0} + \tilde{B}_z$ , the fluctuating component of the Faraday rotation signal takes the form

$$\tilde{\Psi}(\tilde{n}, \tilde{B}_z) = c_F \left( \int \tilde{n} B_{z0} dz + \int n_0 \tilde{B}_z dz \right), \quad (12)$$

where the second order term,  $c_F \int \tilde{n} \tilde{B}_z dz$ , is negligible because both  $\tilde{n}$  and  $\tilde{B}_z$  are small.<sup>13</sup> From this equation we see that the fluctuating part of the Faraday rotation signal is the sum of the fluctuating electron density weighted by equilibrium (poloidal) magnetic field  $\tilde{\Psi}(\tilde{n})$ , and the fluctuating magnetic field weighted by equilibrium density  $\tilde{\Psi}(\tilde{B}_z)$ . For the six central chords (corresponding to  $x \leq 0.3a$ ), density fluctuation contributions are negligible and Eq. (12) can be rewritten as

$$\tilde{\Psi}(\tilde{n}, \tilde{B}_z) \approx \int n_0 \tilde{B}_z dz. \quad (13)$$

The measured Faraday rotation fluctuations for these chords provide a direct line-integrated measurement of magnetic fluctuations. By isolating modes of given helicity, the spatial distribution of the magnetic fluctuations can be determined. These techniques have previously been described in detail and will not be repeated here.<sup>14,15</sup>

Measured line-averaged radial magnetic field fluctuations for the dominant mode ( $m=1, n=6$ ) over a sawtooth cycle are shown in Fig. 5. Maximum amplitude occurs at the crash. The poloidal magnetic fluctuation amplitude measured at the wall is also plotted in Fig. 5, as a dashed line. Radial magnetic field fluctuations have a similar dynamics to poloidal magnetic field fluctuations as is expected for a global tearing mode. The radial magnetic field fluctuation amplitude in the core is approximately three times the poloidal magnetic field at the wall,  $\delta b_r(r) \sim 3 \times \delta b_\theta(a)$ . This approximation simplifies the measurement of particle flux since the inversion of radial magnetic field with fast time resolution is not required.

The resulting spatial profile for the magnetic perturbation of the dominant core-resonant mode ( $m=1, n=6$ ) is

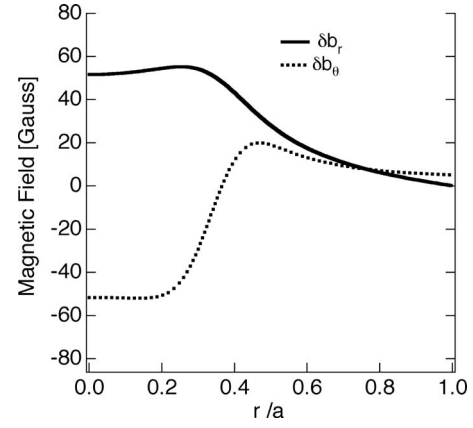


FIG. 6. Radial and poloidal magnetic fluctuation spatial profile for dominant ( $m=1, n=6$ ) mode. Mode resonant surface corresponds to  $r/a \sim 0.35$ .

shown in Fig. 6. At the mode resonant surface ( $r/a \sim 0.35$ ),  $\delta b_\theta = 0$  and  $\delta b_r$  is maximum. Magnetic fluctuations can be tracked in time throughout the sawtooth cycle using the fast Faraday rotation measurements (up to 1 MHz bandwidth) and edge magnetic coils.<sup>14,15</sup>

## V. PARTICLE FLUX MEASUREMENT

The convective electron particle flux from Eq. (3) is given by

$$\Gamma_r^c = V_{\parallel,e} \frac{\langle \delta n \delta b_r \rangle}{B}, \quad (14)$$

and in cylindrical coordinates we can write

$$\nabla \cdot \Gamma_r^c \approx \frac{2V_{\parallel,e}}{B} \left\langle \frac{\partial \delta n}{\partial r} \delta b_r \right\rangle, \quad (15)$$

where  $V_{\parallel,e}$  is the electron parallel mean velocity. In the plasma center  $\delta b_r$  is flat (see Fig. 6), implying  $\frac{\partial \delta b_r}{\partial r} \approx 0$ , and  $\Gamma_r^c/r \approx \partial \Gamma_r^c / \partial r$  is used as  $r$  goes zero.

The electron parallel velocity is determined from equilibrium measurements of the electron density and current density, i.e.,  $V_{\parallel,e} = J_{\parallel,e} / n_e e \approx J_{\parallel} / n_e e$  as shown in Fig. 3, since the mean current along the magnetic field is largely carried by electron motion. Equilibrium magnetic field is determined using an equilibrium fit constrained by Faraday rotation measurements of internal poloidal magnetic field and motional Stark effect measurements of the on axis toroidal magnetic field.<sup>16,17</sup>

To determine the particle transport (and its divergence), one has to measure the phase relation between density fluctuations (density gradient fluctuations) and radial magnetic field fluctuations. Phase measurement is achieved by flux surface ensemble averaging. In MST, rotation of the low- $n$  magnetic modes transfers their spatial structure in the plasma frame into a temporal evolution in the laboratory frame. Since the magnetic modes are global, for convenience we correlate  $\delta n$  (or  $\partial \delta n / \partial r$ ) to a specific helical magnetic mode which is spatially Fourier decomposed from 32 wall-mounted magnetic coils. After averaging over an ensemble of similar events ( $\sim 400$  events are used), we can determine the phase between  $\delta n$  (or  $\partial \delta n / \partial r$ ) and  $\delta b_r$  for the specified

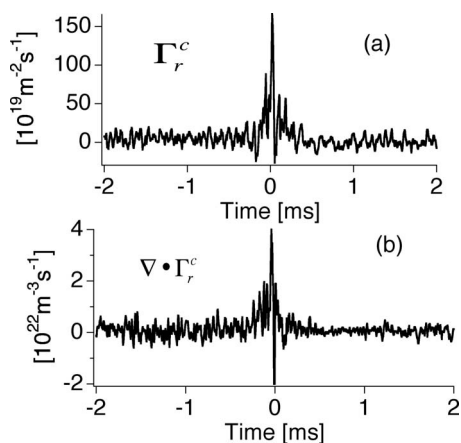


FIG. 7. (a) Convective electron particle flux has a significant increase at sawtooth crash; (b) the divergence of particle flux vs time.  $t=0$  denotes sawtooth crash. The measurement is made at  $r/a=0.11$  near magnetic axis.

mode. For tearing modes, the radial magnetic perturbation has a constant phase over minor radius which has been verified by probe measurements in lower temperature plasmas. Therefore, in reality we correlate density gradient fluctuation to poloidal magnetic field fluctuations measured at the wall to determine the phase. The phase between radial and poloidal component of magnetic field is  $90^\circ$ .

With combined measurements of density fluctuations, density gradient fluctuations, and radial magnetic fluctuations, we are now able to evaluate the flux and its divergence. Using Eq. (14), the direct measurement of convective magnetic fluctuation-induced electron particle flux is shown in Fig. 7(a). It is seen that the particle flux surges, reaching  $\sim 1.0 \times 10^{22} / \text{m}^2 \text{ s}$ , at a sawtooth crash. This corresponds to the time the core density collapse occurs. The positive sign of flux indicates outward particle flux. The divergence of particle flux, determined from Eq. (15), also increases significantly as shown in Fig. 7(b). The divergence of particle flux acts to balance the density change,  $\partial n / \partial t$ .

## VI. SUMMARY

Magnetic fluctuation-induced electron particle flux is measured, for the first time, in the core of high-temperature plasma by combining measurements of equilibrium magnetic field and density with measurements of density, density gradient, and magnetic field fluctuations. For viewing lines

close to the magnetic axis, line-integrated measurements provide good spatial resolution of global fluctuations allowing the local particle flux to be determined. Both the particle flux and its divergence increase significantly at sawtooth crash, corresponding to the fast change in equilibrium density.

## ACKNOWLEDGMENTS

The authors gratefully acknowledge contributions from the MST group. This work is supported by the U.S. Department of Energy.

- <sup>1</sup>P. C. Liewer, Nucl. Fusion **25**, 543 (1985).
- <sup>2</sup>R. J. Bickerton, Plasma Phys. Controlled Fusion **39**, 339 (1997).
- <sup>3</sup>J. M. Finn, P. N. Guzdar, and A. A. Chernikov, Phys. Fluids B **4**, 1152 (1992).
- <sup>4</sup>W. X. Ding, D. L. Brower, D. Craig, B. H. Deng, S. C. Prager, J. S. John, and V. Svidzinski, Phys. Rev. Lett. **99**, 055004 (2007).
- <sup>5</sup>T. E. Evans, R. A. Moyer, P. R. Thomas, J. G. Watkins, T. H. Osborne, J. A. Boedo, E. J. Doyle, M. E. Fenstermacher, K. H. Finken, R. J. Groebner, M. Groth, J. H. Harris, R. J. La Haye, C. J. Lasniers, S. Masuzaki, N. Ohya, D. G. Pretty, T. L. Rhodes, H. Reimerdes, D. L. Rudakov, M. J. Schaffer, G. Wang, and L. Zeng, Phys. Rev. Lett. **92**, 235001 (2004).
- <sup>6</sup>K. H. Finken, S. S. Abdullaev, M. W. Jakubowski, M. F. M. de Bock, S. Bozhenkov, C. Busch, M. von Hellermann, R. Jaspers, Y. Kikuchi, A. Kraemer-Flecken, M. Lehnen, D. Schega, O. Schmitz, K. H. Spatschek, B. Unterberg, A. Wingen, R. C. Wolf, O. Zimmermann, and the TEXTOR Team, Phys. Rev. Lett. **98**, 065001 (2007).
- <sup>7</sup>S. C. Prager, Plasma Phys. Controlled Fusion **32**, 903 (1990).
- <sup>8</sup>I. H. Hutchinson, Principles of Plasmas Diagnostics (Cambridge University Press, New York, 2002).
- <sup>9</sup>S. R. Burns, W. A. Peebles, D. Holly, and T. Lovell, Rev. Sci. Instrum. **63**, 4993 (1992).
- <sup>10</sup>W. X. Ding, D. L. Brower, B. H. Deng, and T. Yates, Rev. Sci. Instrum. **77**, 10F105 (2006).
- <sup>11</sup>H. Soltwisch and H. R. Koslowski, Plasma Phys. Controlled Fusion **37**, 667 (1995).
- <sup>12</sup>N. E. Lanier, D. Craig, J. K. Anderson, T. M. Biewer, B. E. Chapman, D. J. Den Hartog, C. B. Forest, S. C. Prager, D. L. Brower, and Y. Jiang, Phys. Plasmas **8**, 3402 (2001).
- <sup>13</sup>W. X. Ding, D. L. Brower, S. D. Terry, D. Craig, S. C. Prager, J. S. Sarff, and J. C. Wright, Phys. Rev. Lett. **90**, 035002 (2003).
- <sup>14</sup>D. L. Brower, W. X. Ding, S. D. Terry, J. K. Anderson, T. M. Biewer, B. E. Chapman, D. Craig, C. B. Forest, S. C. Prager, and J. S. Sarff, Rev. Sci. Instrum. **74**, 1534 (2003).
- <sup>15</sup>W. X. Ding, D. L. Brower, B. H. Deng, D. Craig, S. C. Prager, and V. Svidzinski, Rev. Sci. Instrum. **75**, 3387 (2004).
- <sup>16</sup>S. D. Terry, D. L. Brower, W. X. Ding, J. K. Anderson, T. M. Biewer, B. E. Chapman, D. Craig, C. B. Forest, R. O'Connell, S. C. Prager, and J. S. Sarff, Phys. Plasmas **11**, 1079 (2004).
- <sup>17</sup>J. K. Anderson, C. B. Forest, T. M. Biewer, J. S. Sarff, and J. C. Wright, Nucl. Fusion **44**, 162 (2004).